Separation and Purification Technology 359 (2025) 130428

Contents lists available at ScienceDirect

Separation and Purification Technology

journal homepage: www.elsevier.com/locate/seppur

Early detection of pore clogging in microfluidic systems with 3D convolutional neural network

Woobin Yi [a,1], Dae Yeon Kim [a,1], Howon Jin [b,*], Sangwoong Yoon [c,*], Kyung Hyun Ahn [a]

[a] School of Chemical and Biological Engineering, Institute of Chemical Processes, Seoul National University, Seoul 08826, Republic of Korea
[b] Chemical Materials Solutions Center, Korea Research Institute of Chemical Technology (KRICT), Daejeon 34114, Republic of Korea
[c] Korea Institute for Advanced Study, Seoul 02455, Republic of Korea

ARTICLE INFO

Keywords:
Pore clogging
Microfluidics
Particle deposition
Machine learning
Artificial intelligence
Convolutional neural network
Clogging forecasting

ABSTRACT

In this study, we investigate whether the clogging phenomenon in a particulate suspension can be predicted from earlier observations of the system. Our research focuses on a microfluidic model system of polystyrene particles dispersed in a glycerol solution, where the onset of clogging can be controlled by adjusting the solution viscosity and flow rate. The microfluidic system allows for optical observations of the flow channels, providing detailed information on how particles are deposited in the flow passage. Using data collected from this model system, we developed a predictive algorithm based on 3D convolutional neural networks (3D CNN) that estimates the probability of clogging onset in the future based on past video frames of the system. Our results show that the 3D CNN can accurately predict clogging even under experimental conditions not encountered during training. The 3D CNN model with a depth of 9 was able to detect clogging after just 25 min, even though the actual clogging occurred after 118 min. This performance is superior compared to the 2D CNN, which detected clogging in 35 min under the same conditions. The high predictive performance indicates that the evolution of particle positions in the early stages of flow contains the necessary information for predicting clogging onset. Our findings have practical implications for the possibility of data-driven predictive maintenance of flow systems.

1. Introduction

In material processing, most of the material moving through the flow path and confined geometry is in a liquid phase. In other words, most of the material processing can be explored as transport phenomena of complex fluids [1]. Complex fluids encompass a wide range of substances, including blood, which is responsible for heat and mass transfer within the living body, and lithium-ion slurry or CMP slurry, which are widely used in the materials industry [2,3]. These fluids share the characteristic of being mixtures of particles or polymers of various sizes. When complex fluids move through a flow path, they often encounter various issues related to transport phenomena in both industrial and academic contexts. Among various issues, clogging is by far the problem that has a severe impact on the process [4].

Clogging is a phenomenon where the flow of particles through a flow path is interrupted, posing a serious issue for process performance and product quality [5]. Particle deposition produced by clogging causes unexpected flow field deformation [6] and vortex formation [7], which in turn impact the accumulation and transport of particles.

Various prior studies on clogging mechanisms have been conducted to understand the causes and processes of clogging that frequently occur in flow processes. Most of these studies have utilized microfluidics, which are easily customizable and allow for the visualization of flow paths. In these microchannels, extensive research has been conducted on mechanisms depending on the size scale of the system [8–10], interactions of particles with flow paths and other particles [4,11,12], and hydrodynamic effects [7,13].

In addition, various methods have been studied to address and improve the clogging phenomenon. For example, backflow reversals and back pulsing methods have been explored, where laminated particle agglomerates are separated and removed from a membrane or flow path by applying an artificial reverse flow [14–17]. In addition, methods such as modifying the surface of the membrane and flow path or using patterned membranes to suppress clogging have been proposed [4,18–20]. However, these methods are difficult to apply in an industrial manufacturing process that operates continuously. Moreover, from the standpoint of productivity and efficiency, it is more important

* Corresponding authors.
E-mail addresses: hjin@krict.re.kr (H. Jin), swyoon@kias.re.kr (S. Yoon).
[1] These authors contributed equally to this work.

https://doi.org/10.1016/j.seppur.2024.130428
Received 20 August 2024; Received in revised form 1 November 2024; Accepted 5 November 2024
Available online 13 November 2024

to predict and respond to clogging in advance than to eliminate it after it occurs.

The approach to clogging prediction may vary based on the clogging mechanism. In cases of rapid clogging [21,22], where impurities larger than the flow path are blocked by size-exclusion, it is possible to predict and solve the clogging by monitoring the size of flowing particles and removing large impurities. On the other hand, it becomes more difficult to predict when progressive clogging occurs due to continuous particle deposition. In this case, it is necessary to continuously monitor the change of the process over a long period. Moreover, it should be also considered that the flow changes due to stacking and instability, which may lead to additional clogging. In many cases, to observe such aggregation-induced clogging, signals such as pressure drop [7], conductivity [23], magnetic resonance imaging [24], and electrical impedance spectroscopy [25–27] in the flow path are visualized and monitored in the form of images and videos. In other words, to effectively respond to a clogging issue in the flow path, a methodology for predicting stable clogging even within the earliest observation time is needed.

As previously mentioned, information about clogging situations can be obtained through various methods, such as the pressure drop within the flow channel, trans-membrane pressure of the membrane, or changes in conductivity. The deposition of particles on the flow channel or membrane can be reflected in these signals through various physical principles, allowing for the collection of large amounts of data by measuring the real-time signals during the flow. In other words, the data measured over time will show differences depending on the occurrence of clogging, and interpreting these differences is essential for predicting and analyzing clogging. However, the differences in signals due to particle deposition and clogging may not be intuitive or visually apparent for human sense, making it important to have the ability to distinguish complex patterns hidden in the signal.

Recently, machine learning has been widely introduced and utilized to address the problem of distinguishing and classifying such complex signals [28–30]. It is also possible, and will be useful to apply these methodologies to the prediction and analysis of clogging, however, such research has rarely been reported to the best of the author's knowledge. A few related studies have explored clogging topics. Lei et al. [31] apply five AI algorithms, including tree-based methods and neural networks, to predict clogging and quantify colloid transport at the pore scale using Lattice Boltzmann simulation data. Ko et al. [32] utilize neural networks to predict pore-scale flow and permeability in heterogeneous porous media, demonstrating high accuracy in velocity field predictions based on synthetic porous structures. The studies mentioned above all rely on simulation results rather than actual clogging outcomes observed in real pores. These works focus on modeling and predicting behavior based on theoretical or simulated data, without incorporating experimental clogging results from real-world porous systems.

Therefore, in this study, we conducted a study to predict pore clogging in microchannels using machine learning. By utilizing deposition image sequences over time from a T-shaped microchannel's particle deposition and clogging, which was conducted in previous studies [13], we aimed to predict future clogging events and develop the most suitable predictive model. Specifically, we evaluated the performance of the model based on a convolutional neural network, which is specialized for image processing, with various input information. Although direct application of this study's findings is challenging in many industrial processes due to the difficulty of obtaining visual data of deposition within flow channels, the significance of this research lies in demonstrating the feasibility of predicting clogging using image data. Furthermore, this study aims to provide a foundation for more challenging research that utilizes indirect signals containing information about particle deposition, such as pressure drop and electrical conductivity, which may have a physical correlation with particle deposition structure.

The paper is organized as follows. Section 2 presents the details of the experiments including microfluidic setup, clogging transition and data preparation for machine learning. Section 3 provides the details of architecture and performance metric of the CNN. Section 4 discusses the effect of time embedding and depth control and presents the results of cross-validation. Section 5 summarizes the results and provides the concluding remarks.

2. Microfluidic model system

2.1. Fluids and microfluidic setup

In this study, we used a suspension of polystyrene (PS) particles well dispersed in an aqueous glycerol solution as the model fluid. Glycerol solution is a typical Newtonian fluid, with medium viscosity that is independent of shear rate, making it suitable for setting the desired medium viscosity and analyzing particle deposition and clogging phenomena under various stress. The dispersed particles were uniform PS beads with a size of approximately $1.5(\pm 0.05)$ μm. The glycerol concentration in the medium with dispersed particles was varied to 50, 60, 70, and 80 wt%. The particle concentration was 0.1 wt%. The prepared samples were labeled according to their glycerol concentration as Gly50PS, Gly60PS, Gly70PS, and Gly80PS.

The prepared samples were injected into a T-shaped microchannel with one inlet and two outlets (Fig. 1). The channels were fabricated using poly(dimethyl siloxane). A syringe pump was used to inject the samples at a constant flow rate through the inlet, and the samples exited through the two outlets exposed to atmospheric pressure. The height of the channel (H), trans-stream width of the channel ($W_{\perp}$), and cross-stream width of the channel ($W_{\parallel}$) were 100, 50, and 100 respectively, with a width ratio of the two outlets of 2:1. Particle deposition and clogging occurring at the T-junction area were captured at 1-minute intervals using a CCD camera focused on a fixed focal plane (the middle plane in the channel height direction). Each sample was tested under five flow rate conditions of 0.7, 1.0, 1.2, 1.5, and 1.7 ml/h. For convenience, these flow rate conditions were labeled as q0.7, q1.0, q1.2, q1.5, and q1.7, respectively. Detailed information about the samples, visualization setup, and channel fabrication can be found in the cited paper [13].

2.2. Clogging transition

The particle deposition patterns varied dramatically with changes in flow rate and glycerol concentration (Fig. 2a). As the flow rate and glycerol concentration increased, the amount of particle deposition gradually decreased. Additionally, under certain flow rate and glycerol concentration conditions, the accumulation of particle agglomerates led to the blockage of the trans-stream outlet of the T-shaped microchannel. In this study, clogging is characterized by the continuous accumulation of particles, which progressively narrows and ultimately obstructs the trans-stream outlet. Although the observed focal plane is at the center of the channel, it is a two-dimensional image, making it difficult to accurately determine clogging in the three-dimensional channel. It is important to note that fluid can continue to flow through pores that are not completely blocked. However, observations from multiple focal planes showed little variation in deposition patterns along the height direction. To classify clogging, image processing was conducted, and detailed procedures can be found in the cited paper [13].

For the Gly50PS and Gly60PS samples, pore clogging occurred at all flow rates due to particle clustering. In the case of Gly70PS, clogging occurred only under the 0.7 ml/hr condition, while no complete clogging was observed at other flow rates. The Gly80PS sample, with the highest glycerol concentration, did not exhibit clogging at any flow rate. Consequently, the clogging phase diagram for each condition is shown in Fig. 2b. In other words, clogging in the T-shaped microchannel was classified into two cases–'clogging' or 'non-clogging'–depending

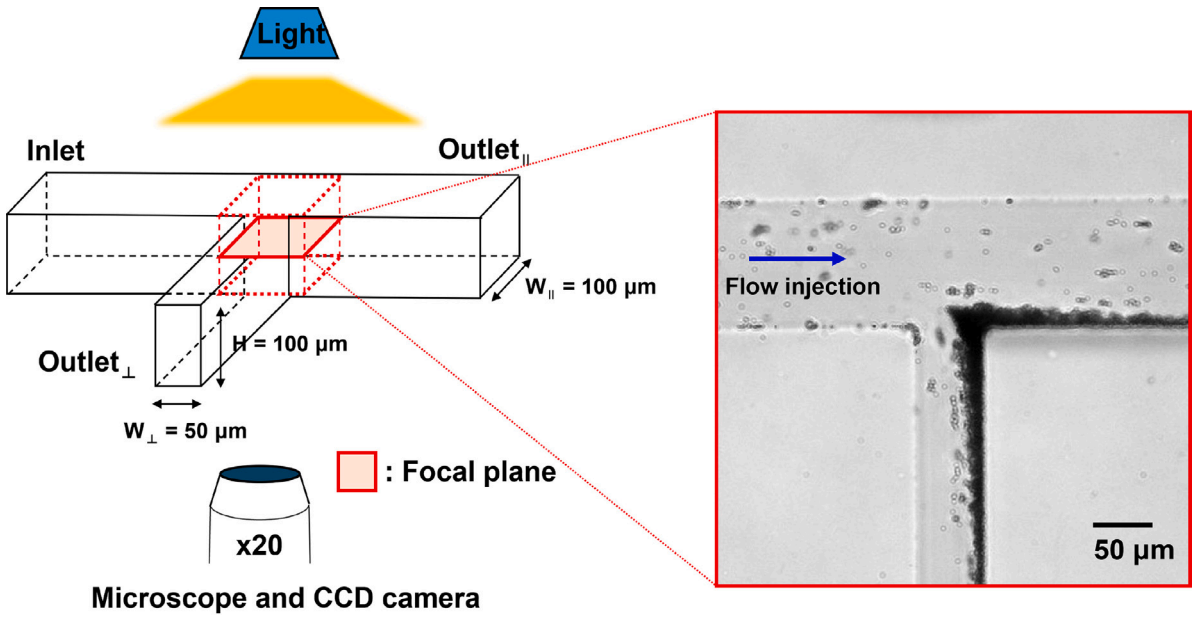

Fig. 1. A schematic of the T-shaped microchannel ($W_{\perp}$: trans-stream width of the channel, $W_{\parallel}$: cross-stream width of the channel, H: height of the channel). Red box is a focal plane where we observed the clogging transition. Focal plane is fixed at the middle region of channel height. Blue arrow shows the flow direction of the injected sample.

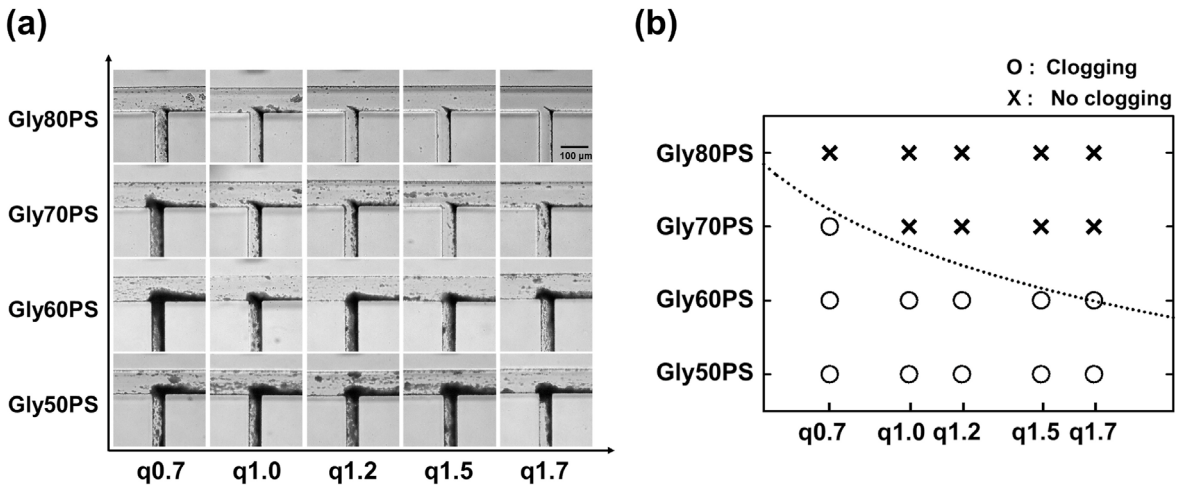

Fig. 2. (a) Clogging behaviors under all flow conditions. (b) Phase diagram of clogging at each flow condition. The dotted line in the graph marks the boundary between clogging and non-clogging.

on the given flow rate and glycerol concentration. The interpretation of clogging transition, along with the classification method for distinguishing between clogging and non-clogging, has been thoroughly explained in our previous work [13]. The clogging transition can be explained by the dynamics of various forces acting on the particles. Specifically, the forces acting on particles flowing around the channel wall where deposition occurs include the body force due to the DLVO potential between particles or between particles and the wall, and the surface force due to the hydrodynamic drag exerted by the flow. The hydrodynamic drag force acts as a detachment force that hinders particle deposition, while the attractive colloidal force acts as an attachment force that promotes agglomerate formation. Thus, in the aggregation-induced clogging mechanism, where continuous particle deposition leads to pore clogging, the balance of these opposing forces determines whether clogging occurs. Both previous and current studies applied various hydrodynamic stresses by changing the medium viscosity and flow rate. The results confirmed that a critical stress value determines clogging, which is a function of the ratio of hydrodynamic drag force to colloidal force [13].

2.3. Dataset preparation for clogging prediction

We constructed a dataset for a machine learning algorithm by capturing images at one-minute intervals using a CCD camera from the microfluidic system described in Section 2.3. This dataset consists of sequences of images continuously taken from the start of flow in each microfluidic channel until the end of the experiment. Each image sequence can be considered as a video capturing the particle deposition process in the microfluidic channel. The experiments were conducted under a total of 20 conditions, comprising five different flow rates and four different glycerol concentrations, among which clogging ultimately occurred in 9 conditions. In the remaining conditions, clogging did not occur (Fig. 2b). Each experimental condition was repeated up to three times, and if repeated, the results were saved as separate videos. We assigned a label of '1' to cases where clogging occurred and '0' otherwise. Next, we constructed a convolutional neural network to perform binary classification to distinguish between images from conditions where clogging occurred and those where it did not. The neural network training was carried out by dividing the experimental data

into two different train-test splits, and the performance was analyzed accordingly.

Each image in the image sequence was preprocessed for efficient artificial neural network computation. The raw data collected from the CCD camera are grayscale images with a resolution of 1000 × 1000 pixels. First, to minimize the impact of brightness variations that might exist in each experiment or recording, the images were binarized. The binarized images were then cropped to 600 × 600 pixels, centered on the channel, to remove any margins. To create a robust model against biases caused by slight differences in camera positioning in each experiment, the position of the crop window was randomly shifted by up to ±60 pixels. Using the cropped 600 × 600 images directly would result in a model with too many parameters relative to the number of training data. Therefore, the images were downsized to 32 × 32 pixels using bicubic interpolation. The compression size was determined as the minimum size that can detect an unblocked channel length of at least 2 pixels in the sample closest to clogging among the non-clogging samples. The minimum size was 32 × 32. Although sizes of 64 × 64 pixels was also tried, there was no significant difference in the overall performance of the model, except a slight increase in accuracy. Therefore, the size of 32 × 32 pixels was chosen as it required the least computational resources. The binarized images compressed to sizes of 32 × 32 and 64 × 64, as well as the uncompressed binarized images, can be found in Figure S1 of the supplementary information. The example images in Figure S1 were obtained from the images of the Gly70PS sample with $q = 1.0$, after 294 min had elapsed. The results of training the model using the binarized images compressed to 64 × 64 are included in Figure S2. It can be observed that increasing the image size does not lead to significant changes in the overall tendency of the model.

To fairly evaluate the performance of the trained model and to verify its ability to generalize to conditions not seen during training, the dataset was divided into train and test datasets based on experimental conditions. Specifically, the experimental conditions present in the train dataset were not included in the test dataset. In other words, each flow rate condition or glycerol concentration appeared exclusively in either the train or test dataset, ensuring a rigorous assessment of the model's generalization performance. This division also aimed to minimize the impact of brightness variations due to different concentrations. All Gly50PS and Gly60PS samples resulted in clogging, whereas all Gly80PS samples were non-clogging. Gly70PS samples were the only ones with mixed clogging and non-clogging cases. Therefore, mixing all images regardless of concentration for train-test splitting posed a risk of the model distinguishing clogging from non-clogging based on subtle brightness differences rather than channel deposition images. Although the images were binarized, to further eliminate any potential influence, Gly50PS, Gly60PS, and Gly80PS images were used for the training dataset, while Gly70PS images were used only for the test dataset. The model's performance was expected to be highest when using Gly70PS images with the most significant flow rate difference (q0.7 for clogging and q1.7 for non-clogging) in the test dataset and lowest when using Gly70PS images with the smallest flow rate difference (q0.7 for clogging and q1.0 for non-clogging). Thus, these two scenarios were named train-test split set 1 and train-test split set 2, respectively. To rigorously evaluate the model's performance, the training dataset was composed exclusively of samples that did not overlap with the test dataset in terms of both flow rate and concentration. Train-test split set 1 comprised 2063 training images and 1193 test images, while train-test split set 2 comprised 1957 training images and 2777 test images.

3. Convolutional neural network for clogging prediction

3.1. Network architecture

In this study, we utilized Convolutional Neural Networks (CNNs) specialized for image data processing. Specifically, we compared the performance of three types of models: a typical 2D CNN, a time-dependent CNN, and a 3D CNN. The neural network structures of these three models differed only in the input processing area according to the characteristics of each model, while the remaining elements were configured identically.

The 2D CNN uses individual images as input (Fig. 3a). This model takes a tensor composed of brightness values from 32 × 32-sized images as input. The input tensor passes through two convolutional layers and max pooling layers, followed by a fully connected layer, ultimately returning a clogging probability between 0 and 1 as the output.

The time-dependent CNN use both image and time information as inputs (Fig. 3b). The time information represents the integer value indicating the number of minutes elapsed since the fluid flow started. This integer value is processed using the positional encoding technique. Positional encoding is a method that transforms integer input values to an encoding vector using sinusoidal functions in order to ensure that the differences between transformed vectors remain consistent, allowing for generalization regardless of the overall length of the input values when training neural networks. Positional encoding represents the input value as a vector composed of multiple sine and cosine functions with different periods. Given an integer time value p, the $2i$-th and $2i + 1$-th dimensions of the positional encoding vector with a size of d_{model}, denoted as $\text{PE}_{(p,2i)}$ and $\text{PE}_{(p,2i+1)}$, can be calculated using the following equations [33]:

$$\text{PE}_{(p,2i)} = \sin(p/10000^{2i/d_{\text{model}}})$$
$$\text{PE}_{(p,2i+1)} = \cos(p/10000^{2i/d_{\text{model}}}) \quad (1)$$

The obtained positional encoding (PE) is used as an input variable along with the image in the time-dependent CNN. Apart from the inclusion of the positional encoding, the time-dependent CNN is identical to the 2D CNN, comprising two convolutional layers, max pooling layers, and a fully connected layer, ultimately returning the clogging probability.

The 3D CNN model stacks 2D images to form a 3D input with a specified depth (d) (Fig. 3c). It takes a tensor of size $d \times 32 \times 32$, composed of images stacked to the depth d, and returns a clogging probability between 0 and 1 as the output. During the training process, the model learns to capture changes in the flow images over time by comparing the stacked images of depth d. This temporal information is also utilized during prediction to enhance the model's performance. Detailed information about the model structures for the 2D CNN, 3D CNN, and time-dependent CNN is provided in Figure S3 of the supplementary information, in the form of PyTorch-style pseudocode.

For model training, we used the Adam optimizer [34] and the Binary Cross-Entropy (BCE) loss function for binary classification of clogging status. To increase computational speed, batch processing was employed, where multiple input values are grouped into a single batch and processed in parallel. The batch size was set to 32, and training continued until the final loss function value was below 0.01. Our model is lightweight and can be trained on CPUs without significant computational resources. We focused on demonstrating the novel application of deep learning to clogging prediction, rather than optimizing performance through extensive hyperparameter tuning.

3.2. Performance metric

The CNN models were designed to predict the probability of clogging. Our model was trained to output a value of 1 for clogging samples and 0 for non-clogging samples. The outputs of our model for previously unseen test inputs are shown in Fig. 4 as an example. For a clogging sample, the probability of clogging increases when later images are used as input compared to non-clogging samples. For non-clogging samples, there is no significant change in the output probability, regardless of whether early or later images are used. Although the clogging probability does not exceed 0.5 even for clogging samples, they can still be distinguished from non-clogging samples by applying a specific threshold value to the output.

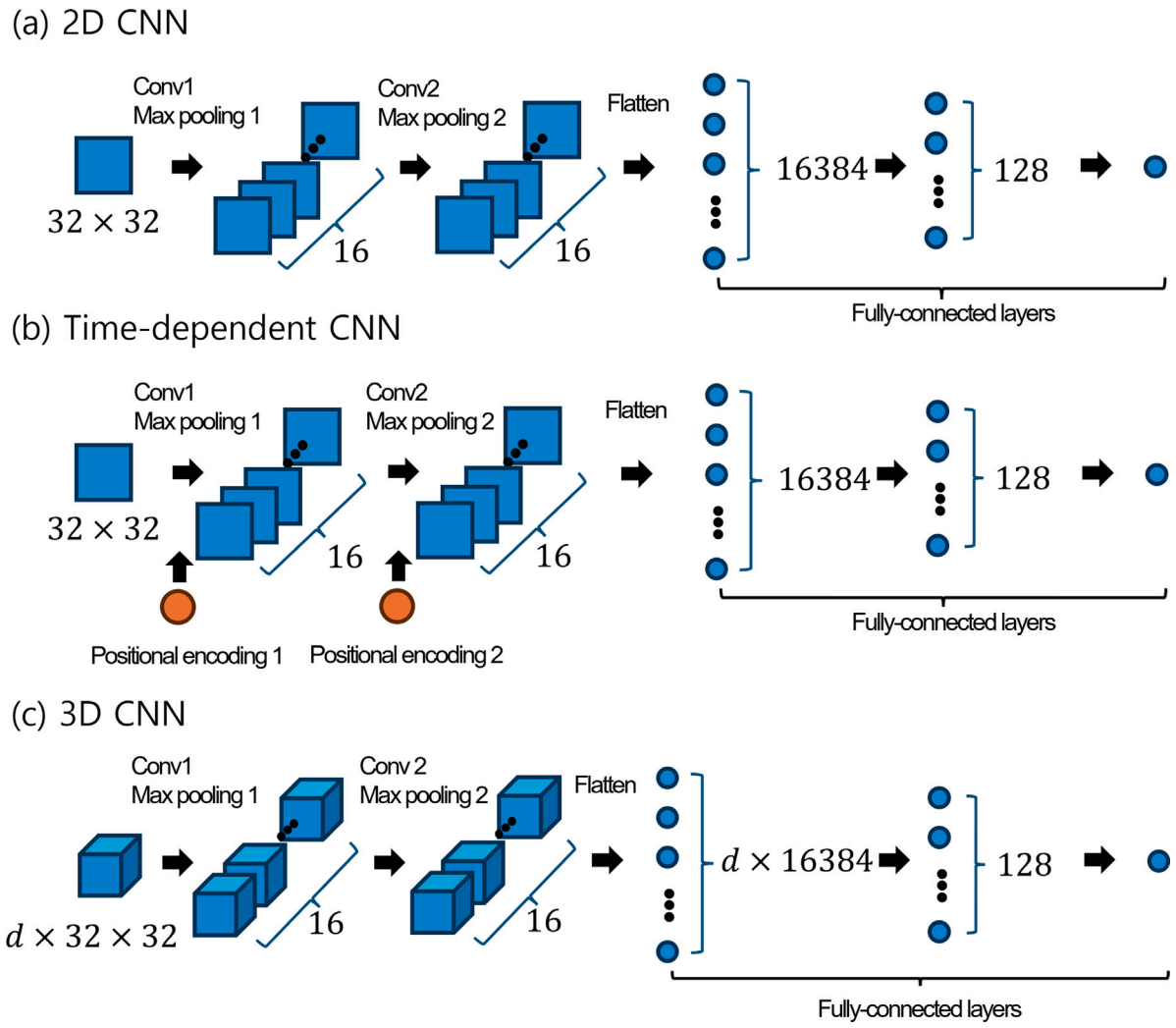

Fig. 3. Architecture of (a) 2D CNN, (b) time-dependent CNN, (c) 3D CNN. Each model shares the same structure, but they differ in their methods of processing time information.

To measure how well the output probability values classify clogging events, we calculated the Area Under the Receiver Operating Characteristic Curve (AUROC). The AUROC is one of the metrics used to evaluate the performance of binary classification models, representing the area under the ROC curve. The ROC curve visualizes the relationship between the model's sensitivity (true positive rate, TPR) and specificity. On the ROC curve, the x-axis represents '1-specificity', and the y-axis represents 'sensitivity'. Sensitivity is the ratio of correctly predicted positive instances to the actual positive instances, while specificity is the ratio of correctly predicted negative instances to the actual negative instances.

$$\text{sensitivity} = \text{FPR} = \frac{\text{FP}}{\text{FP}+\text{TN}}, \quad \text{specificity} = 1 - \text{TPR} = 1 - \frac{\text{TP}}{\text{TP}+\text{FN}} \quad (2)$$

FP stands for false positive (incorrectly predicting positive when it is actually negative), TN stands for true negative (correctly predicting negative when it is actually negative), TP stands for true positive (correctly predicting positive when it is actually positive), and FN stands for false negative (incorrectly predicting negative when it is actually positive). FPR and TPR refer to the false positive rate and true positive rate, respectively. The ROC curve illustrates the relationship between these two rates. The area under the ROC curve (AUROC) increases as the model's ability to distinguish between the two cases improves. Thus, an AUROC value close to 1 indicates excellent predictive performance. The AUROC ranges from 0 to 1, with a value of 0.5 suggesting that the model's predictions are no better than random guessing. Values below 0.5 imply that the model's predictions are inversely correlated with the actual outcomes.

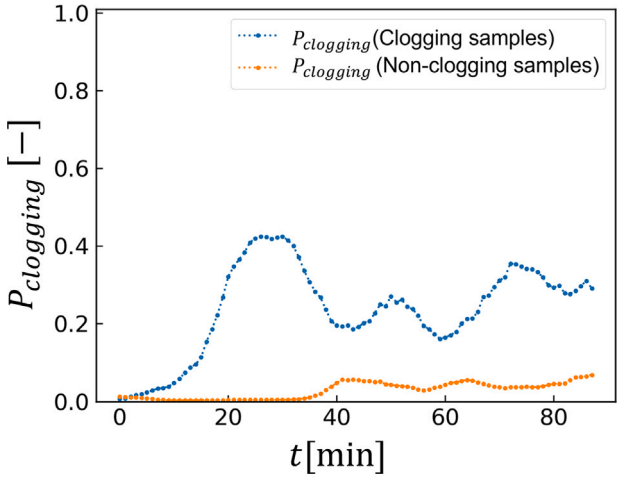

Fig. 4. The clogging probability output values of the model (3D CNN, d = 9) with train-test split set 1. $P_{clogging}$ means the probability of clogging.

While using AUROC allows us to express the model's predictive performance with a single value for a given train-test split set, it does not allow us to track performance changes over time (from early to late flow images). Therefore, to understand how the model's performance changes over time with the variation of input images, we calculated the AUROC values cumulatively at 5-minute intervals. This cumulative AUROC, termed cAUROC, was calculated by accumulating the model outputs every 5 min and plotting these values as a graph. Through the changes in cAUROC values, we were able to quantify the model's performance variations over time.

The point at which the AUROC value first reaches 0.8 was defined as the initial detection time, which implies the time necessary to distinguish the clogging event in the future. This threshold was chosen based on empirical reports indicating that classification results are reliable when the AUROC value is 0.8 or higher [35,36]. For the purpose of comparing the trends in performance differences between models, selecting any sufficiently high AUROC value would yield consistent results. We then observed the changes in initial detection time with varying depths. This allowed us to determine and compare how quickly each model could predict clogging.

4. Result and discussion

4.1. The role of temporal information in clogging prediction

Using 2D CNNs for training and prediction, we investigated whether it is possible to predict clogging in the future based on individual images taken at different times. Fig. 5 shows the cAUROC values for both the 2D CNN and the time-dependent CNN using train-test split set 1. For the initial images taken within the first 10 min, the cAUROC value of the 2D CNN was below 0.6, and it only reached values above 0.8 for the later images taken after 35 min. The low cAUROC value for the early images indicates that the model's performance is not suitable for early prediction of clogging, which is essential for preemptive intervention.

To address this issue, we utilized the time-dependent CNN, which incorporates information about the temporal changes of the stacked images into the model. The time-dependent CNN takes individual images and the time elapsed since the flow started as inputs to ultimately predict whether clogging will occur under the conditions of that image. As shown in Fig. 5, the results of training and predicting using train-test split set 1 indicate that the cumulative AUROC value for the initial images taken within the first 10 min was significantly improved, exceeding 0.8, compared to the 2D CNN. For images taken after 15 min, the cAUROC value approached 1. This demonstrates that the time-dependent CNN performs better than the 2D CNN in predicting clogging using early images. When directly observing the image data, at least at the 15-minute mark, the observer was able to determine the presence of clogging by noting differences in the shape of the accumulated particles. In comparison, the results showing cAUROC values approaching 1 after 15 min can be considered reasonable. A comparison of sensitivity and specificity also shows that the clogging detection performance of the time-dependent CNN is superior to that of the 2D CNN. The graph comparing the sensitivity and specificity of the 2D CNN and the time-dependent CNN can be found in Figure S5a of the supplementary information. Additionally, Figure S2a demonstrates the performance of the 2D CNN and time-dependent CNN when images are compressed to 64 × 64 rather than 32 × 32. When using 64 × 64 images, the cAUROC values increased more rapidly compared to using 32 × 32 images; however, the time-dependent CNN still outperformed the 2D CNN, yielding the same conclusion.

To investigate the role of elapsed time information in the time-dependent CNN, we compared the results by inputting the same image with different time information into the time-dependent CNN trained with train-test split set 1. The altered time input was referred to as t_{alter}. For this purpose, we used the stacked image of the Gly70PS, q1.0 fluid taken 150 min after the flow started. Under this condition, the channel does not clog, so the correct model output should be 0, which implies the probability of clogging (in the future) is zero. However, when we input the counterfactual time value as 1 min, the model output was close to 1. The output began to decrease when the input time value exceeded 25 min, and for times over 75 min, the output was close to 0 (Fig. 6). Between 25 and 75 min, the model output values were between 0 and 1, indicating that the model predicted a moderate probability of clogging under the given input image condition. This demonstrates that the prediction of clogging probability can vary based on the time information, even for the same image. The image used, taken 150 min after the flow started, contains accumulated particles in the channel since the channel ultimately does not clog. If such accumulated particles are present in an early image (within 25 min), the model predicts that more particles will accumulate over time, potentially leading to clogging. However, if the image is from a later time (over 75 min), the model predicts non-clogging since the amount of accumulated particles is relatively small for the elapsed time. This suggests that the time-dependent CNN captures information on how the stacked images change over time based on the input time information and the images themselves. Therefore, including time information as an input is necessary when predicting the likelihood of channel clogging.

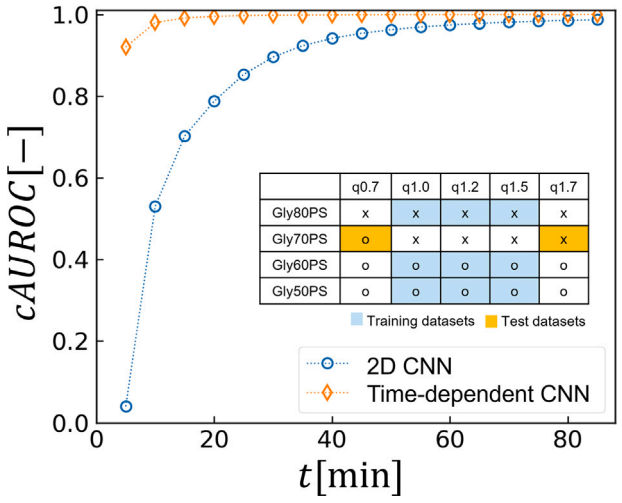

Fig. 5. The cumulative AUROC values for clogging probability in train-test split set 1 using simple 2D CNNs and time dependent CNNs. The measurments are aggregated over 5-minute intervals. In the inset table, "o" indicates a clogging sample, while "x" denotes a non-clogging sample.

4.2. Capturing temporal dynamics using 3D CNN

In the previous section, we demonstrated that information about the elapsed time since the flow started plays a critical role in determining the final clogging status during the channel deposition process. However, in practical scenarios, it may be difficult to accurately measure the elapsed time since the flow started, or it might require very long duration, making it inefficient to directly input time into the neural network. Therefore, using time-dependent CNNs may not be feasible in all situations. To address these challenges, we introduced the 3D CNN, which aims to provide the neural network with indirect information about the passage of time. The 3D CNN is intended to capture the temporal changes in the stacked images purely through the image data itself, without the need for explicit time inputs. This approach allows the network to infer time-dependent changes in the deposition patterns, potentially overcoming the limitations of directly measuring and inputting elapsed time.

The 3D CNN uses images stacked in chronological order up to the depth specified by the model. This allows the network to capture the

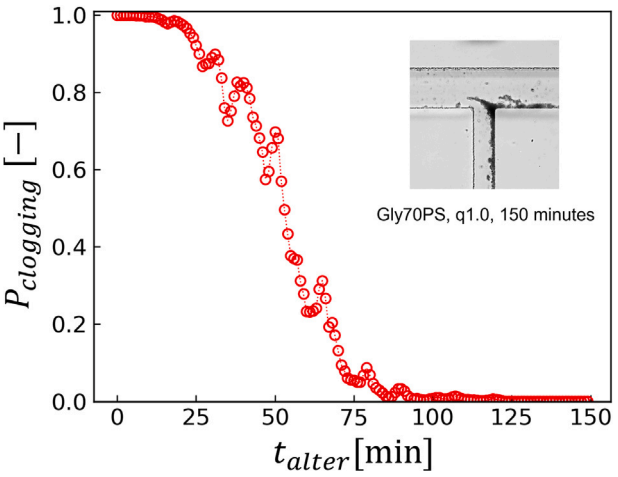

Fig. 6. The clogging probability output values based on time information, with identical image input (Gly70PS, q1.0, 150 min) in time-dependent CNNs. When t_{alter} is small, the probability is close to 1, and as t_{alter} increases, the probability decreases.

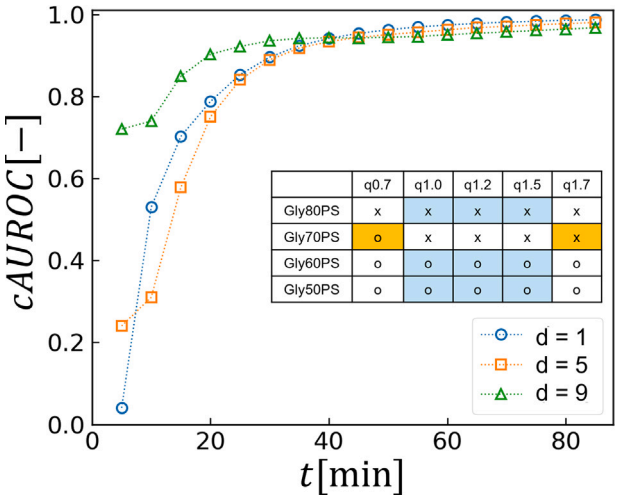

	q0.7	q1.0	q1.2	q1.5	q1.7
Gly80PS	x	x	x	x	x
Gly70PS	o	x	x	x	x
Gly60PS	o	o	o	o	o
Gly50PS	o	o	o	o	o

Fig. 7. The cumulative AUROC values for clogging probability in train-test split set 1 using 3D CNN. The measurements span from d = 1 to d = 9, aggregated over 5-minute intervals. In the inset table, "o" indicates a clogging sample, while "x" denotes a non-clogging sample.

temporal changes in the stacked images. Fig. 7 shows the change in cAUROC values over time for different depths of the 3D CNN. When the depth is 1, the model is equivalent to a 2D CNN. The graph indicates that as the depth increases, the cAUROC value for images up to 5 min also increases. Additionally, for images within 40 min, the model with a depth of 9 achieves the highest cAUROC value regardless of the input image time. For images beyond 40 min, the cAUROC values are very close to 1, irrespective of depth, making the differences due to depth insignificant. The sensitivity and specificity graphs added to the supplementary information also showed the same pattern of model performance improvement with increasing depth, as well as a similar trend where the increase in sensitivity and specificity values slowed down after 40 min (Figure S5b). Figure S2b also presents the cAUROC values for 64 × 64 images. With the improved resolution, the cAUROC values are slightly higher compared to 32 × 32 images; however, the trend remains consistent, with predictive performance increasing as the depth increases.

The improvement in early prediction performance with increasing depth becomes clearer when comparing the initial detection time across different depths. Fig. 8 illustrates the change in initial detection time with varying depths. As depth increases, the initial detection time generally decreases. For a depth of 1, the initial detection time of the 3D CNN is 35 min, whereas, for a depth of 9, it reduces to 25 min. While increasing the depth can enhance prediction performance, it also incurs a cost due to the need to stack images up to the specified depth. Therefore, users can select the depth value that best balances prediction performance and computational cost according to their needs.

The initial detection times of the three models (2D CNN, time-dependent CNN, and 3D CNN) are compared in Fig. 9. When comparing the initial detection times of each model, it is observed that the models detect clogging in the order of time-dependent CNN, 3D CNN, and 2D CNN, from fastest to slowest. In other words, models that can process input data including temporal information are more effective at quickly detecting clogging.

Comparing the initial detection times obtained with 32 × 32 images to those shown in Figures S2a and S2b reveals that detection times are shorter when using 64 × 64 images. Specifically, with 32 × 32 images, the initial detection times for the 2D CNN, time-dependent CNN, and 3D CNNs with depths of 1, 5, and 9 are 35, 5, 35, 35, and 25 min, respectively. When using 64 × 64 images, these times are reduced to 15, 5, 15, 10, and 10 min. This finding suggests that the detailed structural information, such as particle alignment available in higher-resolution images, may contribute to improved clogging detection.

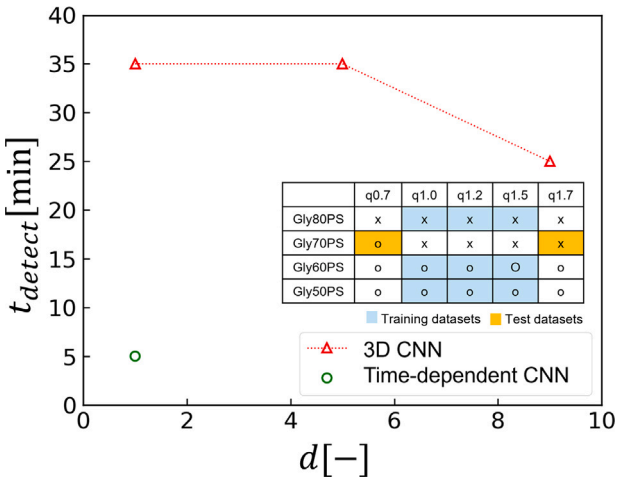

	q0.7	q1.0	q1.2	q1.5	q1.7
Gly80PS	x	x	x	x	x
Gly70PS	o	x	x	x	x
Gly60PS	o	o	o	O	o
Gly50PS	o	o	o	o	o

Fig. 8. The initial detection time in train-test split set 1 for both time dependent CNNs and 3D CNNs. This time marks the point at which the AUROC value surpasses 0.8. In the inset table, "o" indicates a clogging sample, while "x" denotes a non-clogging sample.

4.3. Cross-validation

The results above were consistent across training and test results with different train-test splits. As seen in Fig. 10a, in train-test set 2, the initial cAUROC values for the time-dependent CNN were higher than those for the 2D CNN, similar to train-test set 1. This shows that in train-test set 2, as in train-test set 1, the clogging prediction performance of the time-dependent CNN model, which incorporates temporal information, was superior to that of the 2D CNN which does not incorporate time information. As confirmed in Fig. 10b, the cAUROC values for the 3D CNN also increased with increasing depth in train-test split set 2, similar to train-test split set 1. This indicates that in train-test split set 2, as in set 1, the cAUROC values are highest from the initial images when the depth of the 3D CNN is at its maximum of 9. In both Figs. 10a and b, a slight decrease in cAUROC values was observed after t = 30 min. However, despite this decline, the cAUROC values of the time-dependent CNN remained higher than those of the 2D CNN when t is the same, and the cAUROC values of the 3D CNN increased with increasing depth. A similar pattern can also be

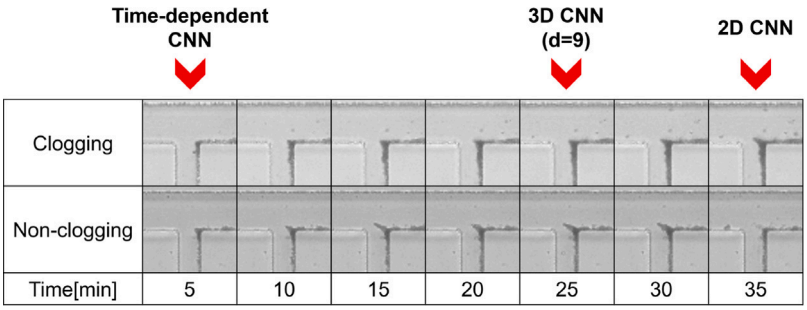

Fig. 9. The initial detection times of the three models depicted in the image frames arranged sequentially over time are as follows: time-dependent CNN, 3D CNN (d = 9), and 2D CNN. The clogging was detected most quickly by the time-dependent CNN, followed by the 3D CNN, and lastly by the 2D CNN.

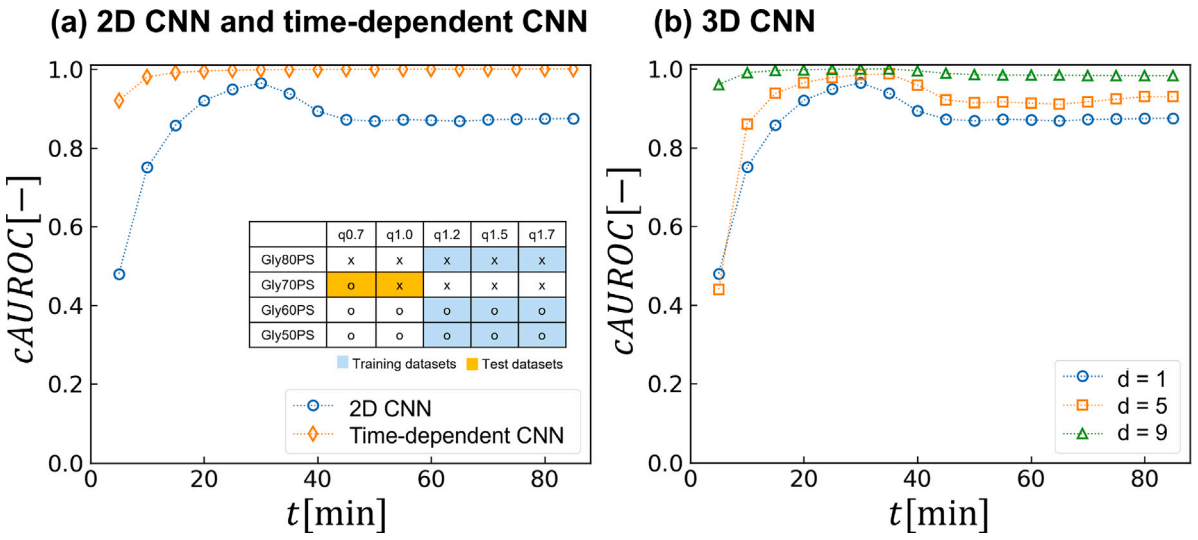

Fig. 10. The cumulative AUROC values for clogging probability in train-test split set 2 using (a) 2D CNN and time dependent CNN, (b) 3D CNN. The measurements span from d = 1 to d = 9, aggregated over 5-minute intervals. In the inset table, "o" indicates a clogging sample, while "x" denotes a non-clogging sample.

observed in the sensitivity and specificity graphs in the supplementary information (Figure S6). Fig. 11 shows the changes in initial detection time depending on the depth of the 3D CNN trained on train-test split set 2. As the depth of the 3D CNN increased, the initial detection time decreased, which is consistent with the results from train-test split set 1.

In summary, the prediction performance for early images within the first 10 min was below a cAUROC of 0.8 for the 2D CNN in both train-test split set 1 and 2. However, the time-dependent CNN exceeded a cAUROC of 0.8 even at the 5-minute mark (Figs. 5, 10a). The initial detection time for the time-dependent CNNs was 5 min for both train-test splits, which is significantly shorter compared to the 35 min (train-test split set 1) and 25 min (train-test split set 2) for the 2D CNNs (Figs. 8, 11). This indicates that incorporating time information along with images is crucial for accurate clogging prediction.

For the 3D CNN, the cAUROC values at a depth of 9 were higher than those at depths of 1 and 5 in both train-test split sets (Figs. 7, 10b). Additionally, the initial detection time was shorter at a depth of 9 compared to depths of 1 and 5 (Figs. 8, 11). Considering that these results were consistent across both train-test split sets, we can infer that the model's performance is robust regardless of the train-test split. Therefore, regardless of the train-test split set used, the CNN model incorporating time information (time-dependent CNN) demonstrated superior predictive performance compared to the 2D CNN. Moreover, using a 3D CNN allowed for earlier prediction of clogging than using a 2D CNN, confirming the same result across different train-test splits. The results of model training on an additional train-test split set can be found in Figure S7 of the supplementary information. Figure S7 shows

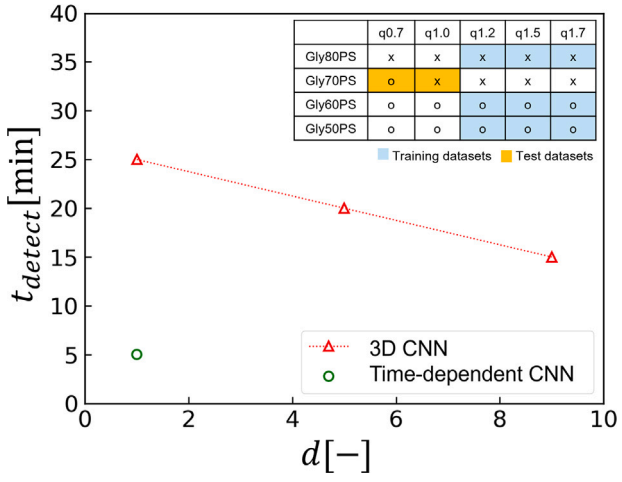

Fig. 11. The initial detection time in train-test split set 2 for both time dependent CNN and 3D CNN. This time marks the point at which the AUROC value surpasses 0.8. In the inset table, "o" indicates a clogging sample, while "x" denotes a non-clogging sample.

that the variety of the training dataset was reduced in order to increase the test dataset. This was unavoidable due to the principle of ensuring that no experimental conditions overlapped between the training and test datasets. While the overall predictive performance decreased as the size of the training dataset was reduced, the models containing more

time information still demonstrated superior performance in predicting clogging.

5. Conclusions

In this study, we introduced convolutional neural networks (CNNs) as a framework for developing models to predict clogging caused by particle deposition. To achieve this, we utilized a T-shaped microchannel that allows for easy observation of the transient clogging process under various hydrodynamic stress conditions. By using time series image sequences classified into cases where clogging occurs and cases where it does not, we trained CNN models to predict the likelihood of clogging from early images alone.

The CNN models used in this study include 2D CNN, time-dependent CNN, and 3D CNN. All three types predict whether the microchannel conditions in the input images will ultimately lead to clogging. The key differences among these models lie in their input data handling: 2D CNN uses single images, time-dependent CNN incorporates both images and the elapsed time since the flow started, and 3D CNN stacks a sequence of images in chronological order to indirectly-capture the temporal changes for prediction.

The results of model training showed that the predictive performance, measured by cAUROC values, improved for all three models, including 2D CNNs, as they processed later images. For the 2D CNNs, the prediction performance for early images within the first 10 min was below a cAUROC of 0.8 in both train-test split set 1 and 2. However, the time-dependent CNNs exceeded a cAUROC of 0.8 even at the 5-minute mark. The initial detection time for the time-dependent CNNs was 5 min in both train-test splits, which is significantly shorter compared to the 35 min (train-test split set 1) and 25 min (train-test split set 2) for the 2D CNNs. This indicates that incorporating time information along with images is crucial for accurate clogging prediction.

For the 3D CNNs, the prediction performance improved with increasing depth. In both train-test split sets, the initial detection time for the 3D CNN with $d = 9$ was 10 min shorter compared to the 2D CNN ($d = 1$). The cAUROC values for images within the first 15 min also increased with greater depth. These results were consistent across different train-test splits.

The results above confirm that it is possible to predict the future possibility of clogging in microchannels. In this study, it was particularly verified that clogging prediction is feasible using only image data. While time-dependent CNNs, which utilize time information in addition to images, are more effective for prediction compared to 2D CNNs that only use images, 3D CNNs, which use only image data, can also predict clogging effectively with increased depth. Thus, incorporating temporal information, whether through time-dependent CNNs or stacking images in 3D CNNs, enhances the predictive performance for channel clogging.

The development of a pore clogging prediction model for microchannels using images in this study extends beyond a simple image classification problem and can be broadly applied to various industrial processes. In actual processes, the properties of liquid materials stored or transported are observed and evaluated as signal images through various sensors. These signal images conceptually correspond to the stacked images used in this study. For example, in the case of pressure signals, it can be inferred that as the flow path becomes clogged, the pressure will rise, and the shape of the flow path will also influence the pressure fluctuation pattern. Clogging may also affect electrical conductivity. Since these scalar signals vary depending on the clogging pattern, it is likely that in the future, clogging could be predicted using scalar signals alone.

It is necessary to develop a model that can be applied to geometries other than T-shaped microchannels by learning from various geometries. However, this study has shown that the stacking patterns of clogging and non-clogging samples exhibit different characteristics, and CNN can detect these patterns at an early stage. The model seems to be capable of distinguishing clogging based on the physical behavior of the system. Since the underlying physics related to clogging remains the same even when the geometry changes, the model would be able to be applied when the geometry changes. From a theoretical perspective, if the model is trained with data from the modified geometry, it would likely exhibit similar classification performance as in this study. Therefore, this research is significant as it presents a framework for predicting changes in material properties in advance, providing a proactive approach to addressing potential issues in process productivity and quality degradation.

CRediT authorship contribution statement

Woobin Yi: Methodology, Investigation, Software, Writing – original draft, Writing – review & editing. **Dae Yeon Kim:** Methodology, Conceptualization, Writing – original draft, Writing – review & editing. **Howon Jin:** Conceptualization, Investigation, Writing – original draft, Writing – review & editing, Supervision, Project administration. **Sangwoong Yoon:** Methodology, Investigation, Software, Writing – original draft, Writing – review & editing, Supervision, Funding acquisition. **Kyung Hyun Ahn:** Supervision, Funding acquisition.

Declaration of competing interest

The authors declare that they have no known competing financial interests or personal relationships that could have appeared to influence the work reported in this paper.

Acknowledgments

This work was supported by the National Research Foundation of Korea (NRF) grant funded by the Korea government (MSIT) (No. NRF-2018R1A5A1024127). S. Yoon is supported by a KIAS Individual Grant (AP095701) via the Center for AI and Natural Sciences at Korea Institute for Advanced Study.

Appendix A. Supplementary data

Supplementary material related to this article can be found online at https://doi.org/10.1016/j.seppur.2024.130428.

Data availability

Data will be made available on request.

References

[1] J. Lee, S. Sung, Y. Kim, J.D. Park, K.H. Ahn, A new paradigm of materials processing—heterogeneity control, Curr. Opin. Chem. Eng. 16 (2017) 16–22.
[2] J.H. Park, C.H. Ahn, K.H. Ahn, Rheological behavior and microstructure formation of Si/C anode slurries for Li-ion batteries, Korea-Aust. Rheol. J. 35 (4) (2023) 335–347.
[3] S. Mukhopadhyay, M.S. Mandal, S. Mukhopadhyay, Pulsatile flow of blood with shear-dependent viscosity through a flexible stenosed artery in the presence of body acceleration, Korea-Aust. Rheol. J. 34 (1) (2022) 17–33.
[4] D.Y. Kim, S.Y. Jung, Y.J. Lee, K.H. Ahn, Effect of colloidal interactions and hydrodynamic stress on particle deposition in a single micropore, Langmuir 38 (19) (2022) 6013–6022.
[5] E. Dressaire, A. Sauret, Clogging of microfluidic systems, Soft Matter 13 (2017) 37–48.
[6] S.Y. Jung, J. Jeong, J.D. Park, K.H. Ahn, Interplay between particulate fouling and its flow disturbance: Numerical and experimental studies, J. Membr. Sci. 635 (2021) 119497.
[7] Y. Kim, K.H. Ahn, S.J. Lee, Clogging mechanism of poly(styrene) particles in the flow through a single micro-pore, J. Membr. Sci. 534 (2017) 25–32.
[8] A. Sauret, E.C. Barney, A. Perro, E. Villermaux, H.A. Stone, E. Dressaire, Clogging by sieving in microchannels: Application to the detection of contaminants in colloidal suspensions, Appl. Phys. Lett. 105 (7) (2014).
[9] G.H. Goldsztein, J.C. Santamarina, Suspension extraction through an opening before clogging, Appl. Phys. Lett. 85 (19) (2004) 4535–4537.

[10] B. Mustin, B. Stoeber, Deposition of particles from polydisperse suspensions in microfluidic systems, Microfluid. Nanofluidics 9 (2010) 905–913.
[11] Z.B. Sendekie, P. Bacchin, Colloidal jamming dynamics in microchannel bottlenecks, Langmuir 32 (6) (2016) 1478–1488.
[12] G.C. Agbangla, P. Bacchin, E. Climent, Collective dynamics of flowing colloids during pore clogging, Soft Matter 10 (33) (2014) 6303–6315.
[13] D.Y. Kim, S.Y. Jung, Y.J. Lee, H. Jin, K.H. Ahn, From successive deposition to clogging of poly (styrene) particles in the cross-flow through a T-shaped microchannel, Sep. Purif. Technol. 322 (2023) 124263.
[14] Y. Gao, J. Qin, Z. Wang, S.W. Østerhus, Backpulsing technology applied in MF and UF processes for membrane fouling mitigation: A review, J. Membr. Sci. 587 (2019) 117136.
[15] W.D. Mores, C.N. Bowman, R.H. Davis, Theoretical and experimental flux maximization by optimization of backpulsing, J. Membr. Sci. 165 (2) (2000) 225–236.
[16] J. Li, D.-R. Chen, S. Li, F. Zhou, Reverse pulsed-flow cleaning for filtration unit regeneration: A review, Sep. Purif. Technol. (2023) 125441.
[17] G. Blandin, H. Vervoort, P. Le-Clech, A.R. Verliefde, Fouling and cleaning of high permeability forward osmosis membranes, J. Water Process Eng. 9 (2016) 161–169.
[18] R. Dehghan, J. Barzin, Membrane patterning through horizontally aligned microchannels developed by sulfated chopped carbon fiber for facile permeability of blood plasma components in low-density lipoprotein apheresis, Sep. Purif. Technol. 278 (2021) 119512.
[19] Y.-J. Won, S.-Y. Jung, J.-H. Jang, J.-W. Lee, H.-R. Chae, D.-C. Choi, K.H. Ahn, C.-H. Lee, P.-K. Park, Correlation of membrane fouling with topography of patterned membranes for water treatment, J. Membr. Sci. 498 (2016) 14–19.
[20] B. Mi, M. Elimelech, Organic fouling of forward osmosis membranes: Fouling reversibility and cleaning without chemical reagents, J. Membr. Sci. 348 (1–2) (2010) 337–345.
[21] O.T. Majekodunmi, S.M. Hashmi, Flow dynamics through discontinuous clogs of rigid particles in tapered microchannels, Sci. Rep. 12 (1) (2022) 22587.
[22] M.A. Eddine, A. Carvalho, M. Schmutz, T. Salez, S. de Chateauneuf-Randon, B. Bresson, S. Belbekhouche, C. Monteux, Sieving and clogging in PEG–PEGDA hydrogel membranes, Langmuir 39 (42) (2023) 15085–15094.
[23] Y. Yoo, S. Moon, Y. Jang, I. Park, H. Lee, M. Lee, A comprehensive investigation of depth filter functionality for a colloidal silica slurry used for semiconductor manufacturing process, IEEE Trans. Semicond. Manuf. 32 (1) (2018) 134–137.
[24] D.G. Von Der Schulenburg, J. Vrouwenvelder, S. Creber, M. Van Loosdrecht, M. Johns, Nuclear magnetic resonance microscopy studies of membrane biofouling, J. Membr. Sci. 323 (1) (2008) 37–44.
[25] J. Kavanagh, S. Hussain, T. Chilcott, H. Coster, Fouling of reverse osmosis membranes using electrical impedance spectroscopy: measurements and simulations, Desalination 236 (1–3) (2009) 187–193.
[26] L. Sim, Z. Wang, J. Gu, H. Coster, A. Fane, Detection of reverse osmosis membrane fouling with silica, bovine serum albumin and their mixture using in-situ electrical impedance spectroscopy, J. Membr. Sci. 443 (2013) 45–53.
[27] J.S. Ho, L.N. Sim, R.D. Webster, B. Viswanath, H.G. Coster, A.G. Fane, Monitoring fouling behavior of reverse osmosis membranes using electrical impedance spectroscopy: A field trial study, Desalination 407 (2017) 75–84.
[28] A. Koesdwiady, R. Soua, F. Karray, Improving traffic flow prediction with weather information in connected cars: A deep learning approach, IEEE Trans. Veh. Technol. 65 (12) (2016) 9508–9517.
[29] A. Samanta, A. Saha, S.C. Satapathy, S.L. Fernandes, Y.-D. Zhang, Automated detection of diabetic retinopathy using convolutional neural networks on a small dataset, Pattern Recognit. Lett. 135 (2020) 293–298.
[30] M.M. Ahsan, S.A. Luna, Z. Siddique, Machine-learning-based disease diagnosis: A comprehensive review, in: Healthcare, Vol. 10, MDPI, 2022, p. 541.
[31] C. Lei, M. Samari-Kermani, H. Aslannejad, A. Zech, Prediction of pore-scale clogging using artificial intelligence algorithms, Stoch. Environ. Res. Risk Assess. 37 (12) (2023) 4911–4919.
[32] D.D. Ko, H. Ji, Y.S. Ju, Prediction of pore-scale flow in heterogeneous porous media from periodic structures using deep learning, AIP Adv. 13 (4) (2023).
[33] A. Vaswani, N. Shazeer, N. Parmar, J. Uszkoreit, L. Jones, A.N. Gomez, Ł. Kaiser, I. Polosukhin, Attention is all you need, Adv. Neural Inf. Process. Syst. 30 (2017).
[34] D.P. Kingma, J. Ba, Adam: A method for stochastic optimization, 2014, arXiv preprint arXiv:1412.6980.
[35] A.P. Bradley, The use of the area under the ROC curve in the evaluation of machine learning algorithms, Pattern Recognit. 30 (7) (1997) 1145–1159.
[36] M.P. Muller, G. Tomlinson, T.J. Marrie, P. Tang, A. McGeer, D.E. Low, A.S. Detsky, W.L. Gold, Can routine laboratory tests discriminate between severe acute respiratory syndrome and other causes of community-acquired pneumonia? Clin. Infectious Dis. 40 (8) (2005) 1079–1086.